Materials Advances

PAPER

Check for updates

Enhanced delivery of polymer beads into cells through arrayed metal nanotubes by the Soret effect†

Kazuhiro Oyama, [iD] Bingfu Liu, Gábor Méhes [iD] and Takeo Miyake [iD] *

Intracellular delivery is crucial for drug delivery, genetic manipulation, and regenerative medicine. Traditional methods such as electroporation are limited by low efficiency and high cell toxicity caused by lipid barriers and endosomal degradation. This can be addressed by developing a gold nanotube (AuNT) stamping system for the direct delivery of beads into adherent cells. The delivery of 200 nm beads through metallic hollow nanotubes occurs within 10 min, which is significantly faster than the 24 h required for endocytosis. Furthermore, controlled temperature gradients based on the Soret effect enhanced the delivery efficiency by up to 152%. Our results demonstrate a significant advancement over conventional techniques while maintaining cell viability above 90% across HeLa, NIH3T3, Hs27, and HCE-T cells. These findings suggest that the AuNT-based stamping system provides a rapid and efficient alternative for intracellular delivery, maintaining high cell viability, while offering precise control over the delivery quantity through temperature gradients.

Introduction

Intracellular delivery refers to the delivery of various signaling molecules into cells for targeted drug delivery and genetic manipulation and plays a crucial role in advancements across various fields ranging from nanomedicine to biotechnology.[1–4] Potential applications include drugs for the treatment of cancer and other diseases, mRNA for viral therapy, and genes with target sequences for gene therapy can be administered. Furthermore, in regenerative medicine, such as in human induced pluripotent stem cells (iPSC), signaling molecules need to be delivered into cells for the activation of specific cellular processes. Thus far, common techniques for intracellular delivery such as patch clamping, electroporation, liposomes, and viral vectors suffer from low delivery rates, low viability, and cell toxicity. This is primarily because the lipidic nature of biological membranes poses a major obstacle to the intracellular delivery of polyionic drugs. Furthermore, after endocytosis, the delivered molecules are often filtered and degraded in lysosomes before fulfilling their roles.[5] Therefore, efficient intracellular delivery requires direct entry into the cytoplasm or avoidance of endosomal compartments such as lysosomes.[1–5]

Diverse methodologies have been developed to overcome the challenges associated with intracellular delivery; however, each has specific limitations. Nanocarriers, such as cell-penetrating peptides, liposomes, cationic lipids, and polymer nanoparticles,[5,6] are usually delivered through physiological approaches. Typically, even large particles, such as those with diameters of ∼100 to 200 nm are readily taken up *via* endocytosis, whereas larger particles require phagocytosis for uptake.[7] Phagocytosis is limited to specialized phagocytic cells, such as macrophages, monocytes, and multinuclear granulocytes.[7,8] However, in endocytosis, where the cargo is wrapped in a lipid bilayer called an endosome, direct intracellular delivery is not considered, and the carried molecules have a high possibility of being digested in the lysosome. Concerning the size of the particles, those with a diameter of 200 nm had higher delivery rates than those with a diameter of 100 nm, which is probably owing to a higher surface area for interaction with cells.[7,8] In addition to the benefit of higher delivery rates, investigations into the intracellular delivery of larger nanoparticles may also open the door to the delivery of large molecules and even organelles. Therefore, there is a need for effective methods of direct intracellular delivery of 200 nm nanoparticles that can avoid the drawbacks associated with endocytosis.

In addition to the above-mentioned physiological methods, direct methods for the intracellular delivery of large nanoparticles include physical penetration into cells by materials

Graduate School of Information, Production and Systems, Waseda University, 2-7 Hibikino, Wakamatsu, Kitakyushu, Fukuoka 808-0135, Japan.
E-mail: miyake@waseda.jp

† Electronic supplementary information (ESI) available. See DOI: https://doi.org/10.1039/d4ma01106f

systems, such as those based on silicon nanowires,[9] diamond nanoneedles,[10] carbon nanofibers,[11] and nanotubes.[5,12] Nanowires and nanoneedles have the advantage of reliable injection into individual cells but are unsuitable for simultaneous delivery to many cells. Nanotubes have emerged as a viable technology that can redefine intracellular substance transport capabilities.[5,12] Connecting an array of hollow metallic nanotubes to a microfluidic channel enables the simultaneous delivery of target substances to multiple cells. Nanotubes were also combined with mechanical,[13] electrical,[14] and photothermal poration,[15,16] although often at the expense of cell viability; for example, voltages exceeding 1.5 V, used for poration, can damage cells by inducing cell-signaling disruptions related to differentiation and reprogramming.[17–20]

To avoid the detrimental effects of electrical and photothermal poration, we recently introduced the physical insertion of nanotubes into cells as a highly efficient intracellular substance delivery method, resulting in high cell viability.[21,22] Our method also allows for the accommodation of large substances, exceeding conventional methods, which are limited to diameters of 100 nm. This is because our nanotubes can have diameters ranging from 0.2 to 2.0 μm, depending on the needs of the substance to be delivered. Furthermore, the diffusion rate of a substance can be increased by utilizing diffusive thermophoresis (also called the Soret effect). Therefore, we have taken an approach to accelerate the delivery rate of beads through nanotubes by utilizing the Soret effect.[23–27] Soret effect refers to the unidirectional thermal diffusion of molecules or particles in the liquid phase along a temperature gradient from high- to low-temperature. As kinetic energy increases with temperature, solutes with a higher density than the solvent move toward the low-temperature side.[23–29] Therefore, the diffusion rate of polymeric signaling molecules with a diameter of 200 nm is expected to increase with increasing temperature owing to the Soret effect.

In this study, we investigated the effects of metal-nanotube-based direct intracellular delivery of polymer beads with a diameter of 200 nm, serving as cargo models for drugs. The metal nanotubes, arranged in an array on an 8 mm polycarbonate substrate, connect directly to multiple adhesive cells through physical penetration. Specifically, we revealed a very promising relationship between the number of delivered beads and the diameter of the nanotubes, as well as the injection time. To maintain high survival rates during prolonged cell penetration, we accelerated the delivery of beads using a temperature gradient between the transmission and reception sides using the Soret effect. During this process, special care was taken to optimize the applied temperatures to prevent any detrimental effects on the cells. Our results demonstrated that the successful direct intracellular delivery of beads using metal nanotube arrays offers a highly promising approach for regenerative medicine and drug delivery. This method not only surpasses natural endocytosis and conventional delivery techniques in terms of the delivery rate and efficiency but also preserves high cell viability and eliminates the dependence on post-endocytic lysosomal metabolic processes.

Experimental section

Fabrication of AuNT membrane stamps

The surface of the track-etched polycarbonate (TEPC) was coated with a tin-palladium metal catalyst layer to form an Au film on the TEPC membrane (it4ip S.A., Belgium), as previously published.[21] Then, the membrane was immersed in a Au plating solution (NC Gold II, Kojima Chemicals) at 40 °C overnight to obtain an Au/TEPC membrane. Like this type of displacement electroless plating technique is well-suited for the microfabrication of Au nanotubes.[30–34] The top surface of the Au/TEPC membrane was etched with aqua regia (ITO-02, Kanto Chemical Co., Inc.) to remove the Au nanolayer, and the TEPC was then etched with O_2 plasma to control the height of the Au NT/TEPC membrane. The Au NT/TEPC membrane was attached to a high-precision flattened glass tube (inner diameter: 7 mm) using a dedicated UV-curable adhesive to create a stamp-like structure.

Cell cultures

HeLa cells (RCB0007; RIKEN BioResource Research Center, Japan), NIH-3T3 (RCB2767; RIKEN BioResource Research Center, Japan), Hs27 (EC94041901-F0; American Type Culture Collection, USA), and HCE-T cells (RCB2280; RIKEN BioResource Research Center, Japan) were used as adherents. The cells were cultured using Dulbecco's Modified Eagle Medium: Nutrient Mixture F-12 (11320033; Gibco|Thermo Fisher Scientific, USA) or modified Dulbecco's Eagle medium (12800017; Gibco|Thermo Fisher Scientific, USA), supplemented with 10% fetal bovine serum (26140079; Gibco|Thermo Fisher Scientific, USA), 0.0588 g L^{-1} penicillin G potassium (P7794; Sigma-Aldrich), and 0.1 g L^{-1} streptomycin sulfate (S6501; Sigma-Aldrich). The cell suspension was obtained using 0.5% trypsin (T4049; Sigma-Aldrich) and dispersed onto 35 cm cell culture dishes or 48-well plates. Finally, the cells were cultured at 37 °C with 5% CO_2 in an incubator. All cell types used were from generations 6 to 17.

AuNT stamping to cells

As described previously, NT stamping of cells was performed using an inverted optical microscope (IX71, IX73, or IX83; Olympus) combined with an x–y–z manipulator.[21,22] The cells were primarily observed using 10×, 20×, and 100× lenses attached to the respective microscopes for image acquisition and NT stamping. The images were captured using a microscope-mounted sCMOS camera (Zyla, Neo, Andor). The NT stamp was inserted into the target cells using a manipulator and observed using differential interference contrast (DIC). First, the focus was adjusted at the bottom and top of the adherent cells to evaluate the average cell height. The focus was carefully lowered from the cell's upper surface to the desired puncture depth (3 μm for HeLa, NIH-3T3, and Hs27; 2 μm for HCE-T), where the NT tip was aligned and inserted into the cell membrane to ensure intracellular penetration. After gently withdrawing the NT from the cells, the sample was returned to a CO_2 incubator and left resting for 20–30 min for cell

membrane repair. Carboxylate-modified microspheres (660 nm (Ex), 680 nm (Em), diameter 0.2 μm, F8807; Thermo Fisher Scientific) were used as beads. Subsequently, the stained samples were treated with fluorescent reagents such as propidium iodide (PI: 16 μg ml^{-1}, P378; Fujifilm Wako Pure Chemical), calcein-AM (16 μM ml^{-1}, C396; Fujifilm Wako Pure Chemical), calcein blue AM acetate (16 μM ml^{-1}, ab275490; Abcam), Hoechst 33342 (405 nm (Ex), 400–450 nm (Em), 16 μg ml^{-1}, H342; Fujifilm Wako Pure Chemical), PlasMem Bright Green (488 nm (Ex), 500–560 nm (Em), 200-fold diluted, P504; Fujifilm Wako Pure Chemical), and PlasMem Bright Red (561 nm (Ex), 560–700 nm (Em), 100-fold diluted, P505; Fujifilm Wako Pure Chemical). EC green endocytosis detection (405 nm (Ex), 500–560 nm (Em)) was used to observe bead uptake through the endocytic pathways. In all cases, fluorescence staining was performed immediately after bead delivery. With EC green endocytosis detection staining, beads that were attached to the cell outer membrane after delivery by NT injection and were not washed off were distinguished by being observed with green fluorescence when delivered into the cell by endocytosis. Stained cells were observed using a fluorescence microscope (IX71, IX73, or IX83; Olympus) or a confocal microscope (FV3000; Olympus) equipped with an sCMOS camera (Zyla, Neo; Andor).

Bead delivery

Here, ϕ200 nm polystyrene beads were adjusted to a concentration of 4.5×10^{10} beads per ml (PBS + 1% bead solution) in PBS. This value was selected based on prior studies employing bead concentrations of, e.g., 2 mg mL^{-1} and 1.5×10^8 beads mL^{-1},[35,36] and preliminary optimization experiments. This concentration provided a balance between preventing aggregation/clogging of the nanotubes and maintaining sufficient bead delivery efficiency. Too low concentrations led to reduced delivery rates, while too high concentrations caused bead aggregation and inconsistent results. Three types of AuNT membranes were used (Fig. 2-a-I–III) with an injection area diameter of 7 mm. HeLa cells cultured within a 7 mm diameter constraint were used for generations 8–16. AuNT injected into cells reached an average depth of 3 μm from the cell top. After injection experiments, the samples were washed three times in Dulbecco's phosphate-buffered saline (DPBS) buffer supplemented with Dulbecco's modified Eagle medium (DMEM) + 10% fetal bovine serum (FBS) and incubated in a CO$_2$ incubator for 30 min for cell membrane recovery. Subsequently, the solution was replaced with a PI solution diluted to 16 μg ml^{-1} in DPBS, incubated for 5 min in a CO$_2$ incubator, washed three times with DPBS, and observed under an inverted fluorescence microscope. The control experiments followed the same procedure. Calcein-AM was adjusted to 16 μM ml^{-1} in DPBS and assayed after the experiment. The observed fluorescence intensity was compared with the control data.

Temperature gradient application in Soret effect experiments

A 500 μl bead suspension or PBS was stored inside a stamp tube. The temperature of these solutions, or the solution in the dish where the cell culture was carried out, along with the stamp tube, was controlled using the following methods. For the 0 °C experiment, the stored solutions in the refrigerator at 4 °C were frozen in a freezer at −20 °C immediately before use and they were used at a temperature of 0 °C. The stamp tubes were stored in a freezer. Temperature control from 20 °C to 45 °C was achieved by placing the solution storage tubes and stamp tube (with PBS) inside a centrifuge tube immersed in a constant temperature water bath set to the desired temperature. This experiment was conducted using quick manual operations at a room temperature of 25 °C.

Results and discussion

Au nanotubes deliver beads directly into the cytoplasm compared to beads trapped in cell membranes during endocytosis

To demonstrate the functionality and advantages of our nanotube delivery system over endocytosis, we performed two sets of experiments using HeLa cells. In the control group, the cells took up the fluorescent polystyrene beads *via* endocytosis. In contrast, in the experimental group, we stamped the same type of beads directly onto the cells using our nanotube injector stamping system, as illustrated in Fig. 1. The essential constituent of the stamping system is an AuNT membrane with nanotubes arranged in an array, similar to a forest of crownless hollow trees (Fig. S1, ESI†); thus, the beads can flow into cells through the NT nanoducts. When we used the nanoinjector with a diameter of 1.0 μm and a nanotube density of 3×10^6 NTs per cm^2, on average of 300 NTs were inserted into the single cell (1000 μm^2) during the delivery.

Confocal bright-field and fluorescence microscopy images revealed apparent differences between the two cell groups, as shown in Fig. 1b. Beads of ϕ = 200 nm, uptaken by endocytosis, tended to intensely concentrate in the intracellular digestive organs around the cell nucleus, as shown by the red fluorescence, originating from Cy5 covalently bonded to the beads (Fig. 1b-I). In contrast, we observed a uniform distribution of fluorescent beads in the cells using the stamping system, strongly indicating that direct delivery into the cells was achieved (Fig. 1b-II). Furthermore, a much shorter time of only ∼10 min was required for the delivery of beads into the cells using our stamping system compared to the relatively long duration of 24 h required for endocytosis. Therefore, using our nanotube system, we succeeded not only in uniform distribution but also in a much faster delivery of beads into the cytoplasm compared to endocytosis, which in turn should result in an overall more efficient delivery process, demonstrating the benefits provided by our nanotube and delivery systems. An advantage of our nanotube stamping system is bypassing the digestive metabolic pathways that severely limit the delivery rates for endocytosis, allowing the target molecules to act effectively within the cell.

Performance analysis of intracellular bead delivery using AuNT/TEPC

Following the results obtained by using 1.0 μm diameter NTs, we investigated the performance of AuNT/TEPCs with three
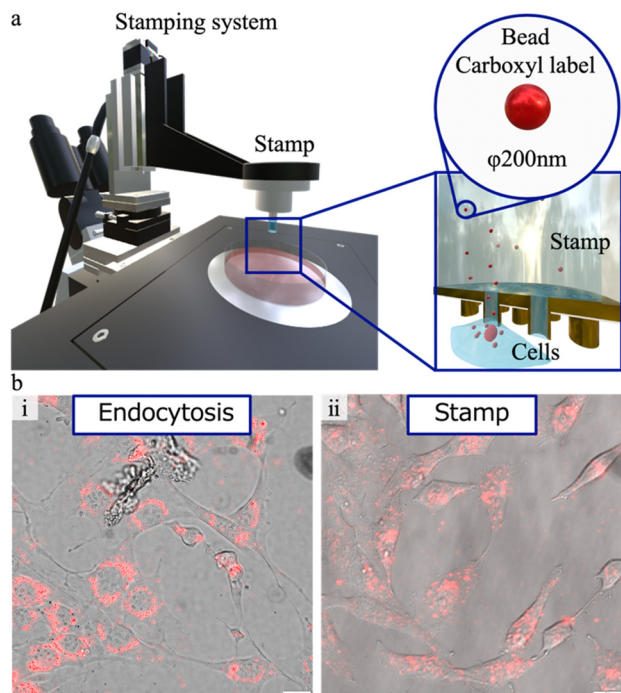
Fig. 1 Bead delivery by the stamping system. (a) Conceptual 3D layout of the stamping system with nanotubes for the intracellular delivery of 200 nm polystyrene beads. AuNTs are highlighted. (b) Overlayed confocal bright field and fluorescence images of polystyrene beads with a diameter of 200 nm, delivered into cells by (i) endocytosis and the (ii) stamping system. The red color in (b) is fluorescence from Cy5-labeled beads. Scale bars: 20 μm.
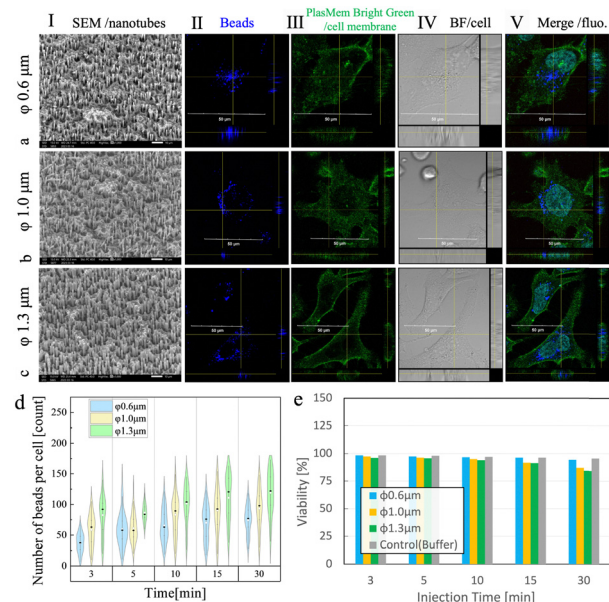

Fig. 2 Bead delivery by AuNT/TEPC. (a–c) For NT diameters of 0.6, 1.0, and 1.3 μm, respectively. (i) SEM images of AuNT/TEPC. Scale bars: 10 μm. Confocal microscopy imaging using (ii) Cy5 filter for beads, (iii) GFP filter for cell membrane stained with PlasMem Bright Green, and (iv) bright field (BF) for cells. (v) Merged images of ii and iii. Horizontal and vertical yellow crossing lines in ii–v represent cross-section areas shown below and to the right of each image, respectively, with a total image height of around 10 μm. Scale bars: 50 μm. (d) Average number of beads delivered per cell at each injection time and (e) viability.

different diameters—0.6, 1.0, and 1.3 μm—for the intracellular delivery of polystyrene beads into HeLa cells. The intracellular delivery of large polystyrene beads with diameters exceeding 100 nm is typically influenced by the surface charge, and anionic carboxyl groups are generally known to be advantageous for cellular uptake.[30,31] Therefore, in this study, carboxyl group-modified polystyrene beads with diameters of 200 nm were used. Experiments were conducted for 3, 5, 10, 15, and 30 min with each AuNT to assess the delivery performance and impact on cells resulting from the differences in the injection time. Cell viability was examined by staining dead cells with the fluorescent dye PI and evaluated using the equation described in our previous studies.[21,22] To confirm that the beads were delivered into the cells, the cell membranes were stained with PlasMem Bright Green.

As observed under a scanning electron microscope (SEM), the inner diameters of the AuNT/TEPC membranes with original template diameters of 0.6, 1.0, and 1.3 μm were 350, 750, and 1000 nm, respectively, while all three versions had the same NT density of 3.0×10^6 cm^2 and the NT height of 5 μm, as shown in Fig. 2a-I, b-I, c-I and Fig. S2 (ESI†). The membranes were assembled in glass tubes to form stamp tubes (Fig. S3, ESI†). The reason for the smaller inner diameters compared to the target diameters (reduction by ∼300 nm) is that a ∼150 nm gold layer was plated inside the pores of the TEPC membrane and pores with diameters equal to those of the target

diameters. In this study, HeLa cells were used as a human cervical cancer cell line. HeLa cells in a dish-adherent state have a height of 5–8 μm; therefore, the depth of nanotube penetration was controlled to be 2–3 μm with the nanotube length adjusted to 5 μm. The delivery of beads into the cells was verified by confocal microscopy for each nanotube diameter (Fig. 2, using a (II) Cy5 filter for beads, (III) GFP filter for cell membranes stained with PlasMem Bright Green, (IV) bright field (BF) for cells, and (V) merged fluorescence images of II and II–IV). From figures a–c (V), we can see that the beads marked in blue (corresponding to Cy5) are located inside the cell membrane, which is marked in green (corresponding to GFP). Therefore, we confirmed that NTs of each diameter could be used to deliver beads directly into the cells.

To quantify the efficiency and feasibility of the delivery, we counted the number of delivered beads using each AuNT variant at each injection time (Fig. 2d), calculated the distribution of delivered beads per cell for 10 min (Fig. S3, ESI†), and estimated the cell viability (Fig. 2e) after delivery. Bead counts and subsequent bead distributions were estimated by recording the Cy5 fluorescence inside each cell observed from the 3D images by confocal microscopy. As expected, the bead counts increased with the delivery time and nanotube diameter (Fig. 2d). For example, at the injection time of 10 min, the median of bead counts from the violin plot were 63, 90, and 104 for 0.6 μm, 1.0 μm, and 1.3 μm nanotubes, respectively. Notably, based on the relatively high bead count at an injection

time of 3 min, we inferred that many of the beads had already been released into the cells at the time of insertion. Furthermore, based on the distribution of beads per cell observed at 10 min, both of the smaller tubes with diameters of 0.6 μm and 1.0 μm delivered fewer beads (41–60 beads to most cells, followed by 61–80 beads), compared to 1.3 μm tubes (61–80 beads to most cells, followed by 81–100 beads), pointing at a limitation related to tube diameter. Contrary to cell counts, cell viability (Fig. 2e) consistently showed high values of over 90%, except for extended nanotube injection times of 30 min for tube diameters of 1.0 and 1.3 μm, when the viability dropped to ∼ 80%, which is still a sufficiently high value. For both observations, injection and control experiments were conducted in DPBS for the same duration of placement in DPBS. At an injection time of 10 min, the viability was 97% for 0.6 μm nanotubes, 95% for 1.0 μm, and 94% for 1.3 μm NTs.

While the NT diameter and injection time were positively correlated with the number of beads delivered for 3–30 min, this was not true for 0–3 min. The reason for this may be the release of many beads immediately after NT injection. This was likely due to the initial rapid diffusion driven by the concentration gradient and cytoplasmic streaming (CPS). When a high-concentration bead solution contacts a bead-free intracellular fluid, a steep concentration gradient causes a rapid diffusion flow, which is most intense immediately after contact and gradually slows over time. Additionally, the CPS, driven by the movement of the cytoskeleton and intracellular substances, aids in bead uptake immediately after NT insertion. However, a few minutes post-injection, the cytoskeletal polarity shifts towards the NT penetration site for cell membrane repair, altering the flow to suppress further diffusion and making Brownian motion the dominant diffusion mechanism.[37–40] Furthermore, cell viability was expected to decrease significantly with longer injection times, but it showed sufficient values of over 80%. However, when trying to increase the number of beads delivered by increasing the NT diameter and increasing the injection time to 30 min, the cell activity and viability dropped from the 90% range to the 80% range. This probably originated from the accumulating damage to the intracellular environment over 30 min of injection time. The inserted NTs extracted the molecules from the cells after 30 min. A duration of 30 min appears to be an important biological factor. Typically, when pores are formed in the cell membrane, the cell's wound-healing mechanisms are activated, involving the reconstruction of the cytoskeleton and the accumulation of polarity-regulating proteins at the damaged site. Subsequently, new cell membrane synthesis ensures stable repair. This response occurs within 30 min.[40] Therefore, if normal cell polarity switching and wound healing do not occur within 30 min of damage, there is a high likelihood of cell death. If NTs continue to penetrate the cell membrane for 30 min, cellular wound healing mechanisms may become impaired. Larger NT diameters enable the delivery of more beads, providing increased efficiency for certain applications. On the other hand, while NT diameters exceeding 1.3 μm have the potential to reduce cell viability due to mechanical stress,

this effect is closely linked to the duration of NT insertion. Our findings indicate that when the NT insertion time is short, the impact of diameter on cell viability is negligible. However, with prolonged insertion times, such as 30 min, larger NT diameters lead to a noticeable decrease in cell viability. Therefore, the NT diameter and insertion time should be carefully optimized to balance the delivery efficiency and cell viability based on the specific application. Compared to conventional electroporation techniques, which typically achieve a cell viability of ∼ 80%,[41–43] the AuNT-based method presented here demonstrated a consistently higher viability of over 90%, as shown in Fig. 2e. These results highlight the potential advantage of the AuNT-based approach in preserving cell viability during intracellular delivery.

Acceleration of intracellular bead delivery by the Soret effect

To deliver more beads into the cells without extending the delivery time or further increasing the NT diameter, which could negatively affect cell viability, bead delivery was accelerated using the Soret effect. Specifically, we utilized temperature-gradient-based thermodiffusion as an accelerating force for bead flow by increasing the temperature of the delivery solution in the glass tube compared to the lower temperature of the dish-side solution containing the cells. The Soret flux ($J_{soret,i}$) is represented by the product of the diffusion flux generated by the concentration gradient (J_i), described by Fick's law in eqn (1), by the diffusion flux generated by the temperature gradient (J_q), described by Fourier's law in eqn (2), and expressed in eqn (3):

$$J_i = -D_M \frac{dC_i}{dx} \tag{1}$$

$$J_q = -\lambda \frac{dT}{dx} \tag{2}$$

$$J_{soret,i} = -D_T C_i \frac{dT}{dx} \tag{3}$$

where D_M represents the diffusion coefficient of a substance, C_i represents the concentration, x represents the spatial coordinate, t represents the time, λ represents the thermal conductivity, and T represents the temperature. Additionally, D_T is the thermal diffusion coefficient.

$$J_{total} = J_i + J_{soret,i} \tag{4}$$

This can be written concretely as eqn (5).

$$J_{total} = -D_M \left(\frac{\partial C_i}{\partial x} \right) - D_T C_i \left(\frac{\partial T}{\partial x} \right) \tag{5}$$

Fig. 3a depicts the concept of bead delivery by the Soret effect. The temperature of the 500 μL bead suspension buffer in the stamp tube was controlled to create a temperature difference with the culture cell dish, to accelerate intracellular bead delivery. All experiments involved the penetration of cells with nanotubes for 10 min and the simultaneous delivery of temperature-adjusted bead suspensions. After penetration, the cells were incubated in a CO_2 incubator for 30 min to allow membrane self-repair. Subsequently, cell viability was measured
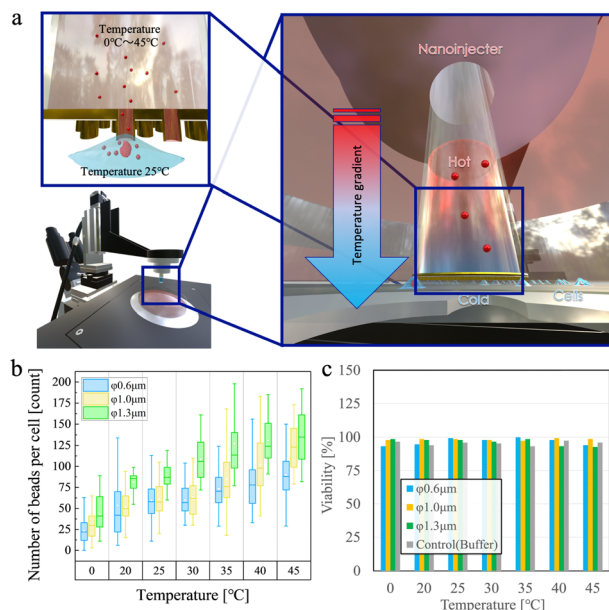
Fig. 3 Bead delivery using the temperature gradient. (a) 3D illustration of temperature gradient-accelerated bead delivery using a stamping system. (b) Number of beads delivered per cell *versus* temperature of delivery solution, (c) and viability.

using the PI dye, and the number of beads inside each cell was determined. The culture dish on the cell side was set to room temperature (25 °C), and the temperature of the stamping solutions was varied from 0 to 45 °C in 5° increments for each of the three types of nanotube membranes for the temperature tests. The temperature gradient was optimized to enhance the Soret effect, improving bead diffusion into cells while maintaining cellular safety. Gradients exceeding 5 °C were necessary for significant enhancement, while a range from 0 °C to 45 °C (in 5 °C increments) was tested to identify the optimal balance between delivery efficiency and minimizing stress on cells and their proteins.

Fig. 3b shows the median number of beads delivered per cell. At an injection temperature of 0 °C, the number of delivered beads was 22, 31, and 41 for nanotubes with diameters of 0.6, 1.0, and 1.3 μm, respectively. Increasing the temperature increased the number of beads delivered into the cells linearly. At the highest set injection temperature of 45 °C, the fluorescence intensity corresponded to 88, 126, and 133 beads for nanotubes with diameters of 0.6, 1.0, and 1.3 μm, respectively. Each of these delivery conditions was found to allow a high cell viability above 90% (Fig. 3c), indicating high cell survival rates.

As the medium temperature was set to 25 °C, setting the injection temperature *via* nanotubes also to 25 °C did not produce the Soret effect, as shown in eqn 5; in other words, bead delivery occurred solely through simple diffusion. The Soret effect is achieved by decreasing or increasing the injection temperature to a set medium temperature. In our system, the Soret effect induced by a temperature gradient caused beads to migrate from the higher temperature regions to the lower temperature regions Taken together, incorporating the Soret

effect-driven thermodiffusion accelerating force into the stamping system improved the delivery efficiency of polymer beads into cells. A 10-min injection with the delivery side set at a temperature 20 °C higher compared to the dish side solution resulted in a ~1.5-fold increase in the number of beads compared to not using a temperature gradient.

Bead delivery to various types of cells

To demonstrate the compatibility of our NT-based stamping method with various cell types, we compared the bead delivery into HeLa cells (Fig. 4a) with deliveries into cell lines of mouse fibroblasts NIH-3T3 (Fig. 4b), human neonatal foreskin cells Hs27 (Fig. 4c), and human corneal epithelial cells HCE-T (Fig. 4d) using the $\phi 1.0$ μm (inner diameter: 750 nm; density: 3.0×10^6 cm^2; height: 5 μm) nanotube membranes. The cells were punctured with PBS + 1% bead solution for 10 min, and the temperature was adjusted to 25 °C on both the delivery and receiving sides.

Fig. 4a–d show the fluorescence images obtained by confocal microscopy, where beads are marked in blue (dark red fluorescence with a Cy5 filter), cell membranes are marked in red (red fluorescence stained with PlasMem Bright Red with a RFP filter), endosomal membranes are marked in green (green fluorescence stained with EC green endocytosis detection with a GFP filter), and cell nuclei are marked in cyan (blue fluorescence stained with Hoechst 33342 with a DAPI filter). In all cases, fluorescence staining was performed immediately after bead delivery. We observed that HeLa and NIH-3T3 cells had similar amounts of fluorescence signals corresponding to
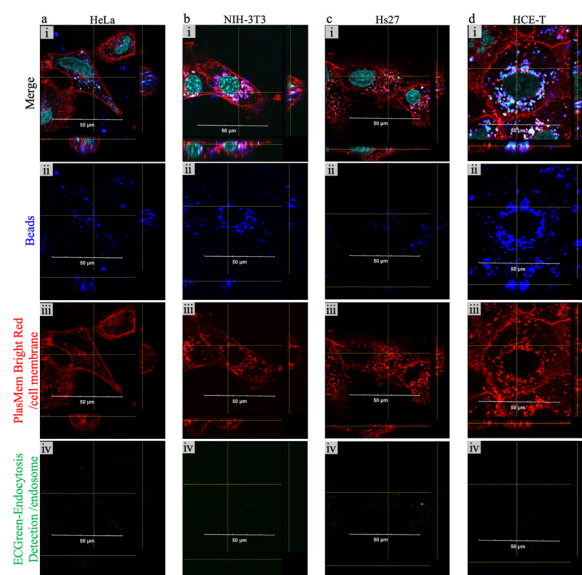

Fig. 4 Bead delivery using stamping to (a) HeLa, (b) 3T3, (c) Hs27, and (d) HCE-T cells. For each image in a–d: (i) merged fluorescence images from ii–iv; (ii) beads observed with Cy5 filter; (iii) cell membrane stained with PlasMem Bright Red observed with RFP filter; (iv) endosomes stained with EC Green-Endocytosis Detection observed with GFP filter. Horizontal and vertical yellow crossing lines in a–d represent cross-section areas shown below and to the right of each image, respectively, with a total image height of around 10 μm. Scale bars: 50 μm.
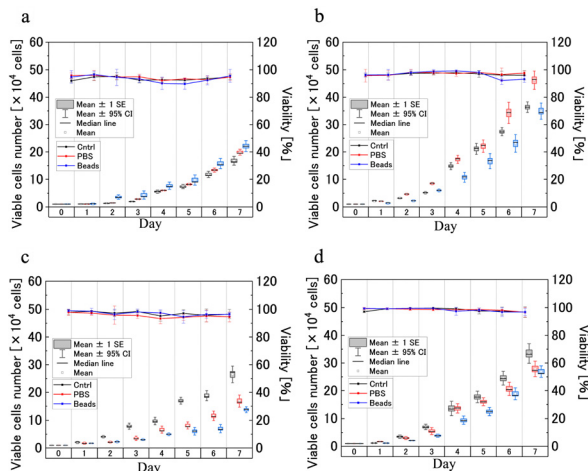
Fig. 5 Growth curve and viability of each cell type. (a) HeLa, (b) 3T3, (c) Hs27, and (d) HCE-T cells. Line graph is the viability. The box plot graph is the growth curve. Line graphs represent the mean ± 1 standard error. Boxes in box plot graphs represents the mean ± 95% confidence interval.

intracellularly delivered beads, with NIH-3T3 cells having slightly fewer beads per cell owing to the average size difference between the two cell lines. Initially, Hs27 cells showed similar results to NIH-3T3 cells, but the number of beads inside the cells decreased during the staining and observation process. This was likely due to the rapid metabolism of newborn foreskin cells. In all cases, the lack of a signal in endosome-stained images viewed with a GFP filter indicated that beads were not internalized by endocytosis, proving successful delivery by our stamping system.

Fig. 5a–d represent each cell type's growth and viability curves observed over 7 days. Three experiments were conducted for each cell type: stamp delivery with PBS + 1% bead solution, stamp delivery with PBS only, and the non-stamped control. Each data point represents the average of at least three samples. All the tested cell types exhibited a gradual cell proliferation trend in all conditions, with somewhat faster growth for HCE-T and a relatively rapid growth for NIH-3T3. According to Fig. 5c, showing Hs27 cells, although young fibroblasts show a growth curve similar to that of HeLa cells, there are minor differences observed among the two stamped and the control samples that are likely influenced by the initial cell numbers. Compared to other cell types, the viability does not significantly decline over time, with all data consistently >80%. Although there are slight differences in the curves between the two stamped samples and the control samples, these differences fall within the normal range. Additionally, there were no samples with significantly low cell viability. Fig. 5d reveals that HCE-T cells, known for their relatively slow growth rate, exhibited accelerated growth based on the cell growth curve, maintaining high cell viability even after several days. These results demonstrated that NTs can deliver polymer beads to various cell types such as cancer cells, fibroblasts, and corneal epithelial cells, while maintaining high viability and good cell growth over the observed period of 7 days.

Conclusions

We explored the AuNT/TEPC stamping system for the delivery of 200 nm diameter beads, as a model of large substances into adherent cells. The 200 nm beads were successfully delivered into HeLa cells using our stamp, with a positive correlation between the NT diameter and injection time. Therefore, careful selection of these two parameters is essential to achieve the desired number of deliveries into cells. Moreover, in the accelerated bead delivery experiment utilizing the Soret effect, we succeeded the increase in the number of delivered beads into cells with over 90% viability even if we exceed 45 °C temperature on the nanotube side. Furthermore, bead delivery to various cell types, namely, HeLa, NIH3T3, Hs27, and HCE-T cells, was achieved without affecting cell growth over a 7-day period. This study highlights the potential of nanotubes for intracellular delivery of large cargos, such as 200 nm beads, and suggests the feasibility of extending this approach to even larger cargos, including organelles or high-molecular-weight therapeutics. Additionally, as demonstrated in our reference study, NT stamps with a diameter of 18 mm can simultaneously process over 3×10^5 cells, underscoring its potential scalability for clinical applications.[44] Future research will focus on addressing challenges related to biocompatibility, long-term safety, and *in vivo* applicability. Automating the NT stamping process and integrating it into high-throughput systems could further enhance its utility for regenerative medicine, intracellular drug delivery, and genetic manipulation. These advancements could significantly contribute to improved patient outcomes and reduced healthcare costs, paving the way for clinical translation.[45–47]

Author contributions

Kazuhiro Oyama: conceptualization, data curation, formal analysis, investigation, methodology, project administration, validation, visualization and writing – original draft & editing. Bingfu Liu: validation. Gábor Méhes: funding acquisition, supervision and writing – review & editing. Takeo Miyake: funding acquisition, methodology, project administration, supervision and writing – review & editing.

Data availability

All newly generated data are presented in the manuscript and the ESI.† The raw data will be posted on the BOX website after the publication.

Conflicts of interest

There are no conflicts to declare.

Acknowledgements

References

1 S. Carregal-Romero, E. Caballero-Díaz, L. Beqa, A. M. Abdelmonem, M. Ochs, D. Hühn, B. S. Suau, M. Valcarcel and W. J. Parak, *Annu. Rev. Anal. Chem.*, 2013, **6**, 53–81.

2 K. B. Cederquist, S. L. Dean and C. D. Keating, *Wiley Interdiscip. Rev.: Nanomed. Nanobiotechnol.*, 2010, **2**, 578–600.

3 T. Sen and I. J. Bruce, *Sci. Rep.*, 2012, **2**, 564.

4 J. N. Anker, W. P. Hall, O. Lyandres, N. C. Shah, J. Zhao and R. P. Van Duyne, *Nat. Mater.*, 2008, **7**, 442–453.

5 A. Prokop, *Intracellular Delivery Fundamentals and Applications*, Springer, Netherlands, Dordrecht, 1st edn, 2011.

6 H. Nakamura and S. Watano, *KONA Powder Part. J.*, 2018, **35**, 49–65.

7 W. Zauner, N. A. Farrow and A. M. R. Haines, In vitro uptake of polystyrene microspheres: effect of particle size, cell line and cell density, 2001, **1**, 39–51.

8 S. Chono, *Yakugaku Zasshi*, 2007, **127**, 1419–1430.

9 M. Rabinovitch, *Trends Cell Biol.*, 1995, **5**, 85–87.

10 W. Kim, J. K. Ng, M. E. Kunitake, B. R. Conklin and P. Yang, *J. Am. Chem. Soc.*, 2007, **129**, 7228–7229.

11 Y. Wang, Y. Yang, L. Yan, S. Y. Kwok, W. Li, Z. Wang, X. Zhu, G. Zhu, W. Zhang, X. Chen and P. Shi, *Nat. Commun.*, 2014, **5**, 4466.

12 T. E. McKnight, A. V. Melechko, G. D. Griffin, M. A. Guillorn, V. I. Merkulov, F. Serna, D. K. Hensley, M. J. Doktycz, D. H. Lowndes and M. L. Simpson, *Nanotechnology*, 2003, **14**, 551–556.

13 J. J. VanDersarl, A. M. Xu and N. A. Melosh, *Nano Lett.*, 2012, **12**, 3881–3886.

14 C. Chiappini, E. De Rosa, J. O. Martinez, X. Liu, J. Steele, M. M. Stevens and E. Tasciotti, *Nat. Mater.*, 2015, **14**, 532–539.

15 X. Ding, M. P. Stewart, A. Sharei, J. C. Weaver, R. S. Langer and K. F. Jensen, *Nat. Biomed. Eng.*, 2017, **3**, 39.

16 T. Man, X. Zhu, Y. T. Chow, E. R. Dawson, X. Wen, A. N. Patananan, T. L. Liu, C. Zhao, C. Wu, J. S. Hong, P.-S. Chung, D. L. Clemens, B.-Y. Lee, P. S. Weiss, M. A. Teitell and P.-Y. Chiou, *ACS Nano*, 2019, **13**, 10835–10844.

17 G. A. Vinnacombe-Willson, N. Chiang, L. Scarabelli, Y. Hu, L. K. Heidenreich, X. Li, Y. Gong, D. T. Inouye, T. S. Fisher, P. S. Weiss and S. J. Jonas, *ACS Cent. Sci.*, 2020, **6**, 2105–2116.

18 J. Teissié, N. Eynard, B. Gabriel and M. P. Rols, *Adv. Drug Delivery Rev.*, 1999, **35**, 3–19.

19 W. Kang, J. P. Giraldo-Vela, S. S. P. Nathamgari, T. McGuire, R. L. McNaughton, J. A. Kessler and H. D. Espinosa, *Lab Chip*, 2014, **14**, 4486–4495.

20 R. Adam Seger, P. Actis, C. Penfold, M. Maalouf, B. Vilozny and N. Pourmand, *Nanoscale*, 2012, **4**, 5843–5846.

21 B. Zhang, Y. Shi, D. Miyamoto, K. Nakazawa and T. Miyake, *Sci. Rep.*, 2019, **9**, 6806.

22 B. Zhang, D. Zheng, S. Yiming, K. Oyama, M. Ito, M. Ikari, T. Kigawa, T. Mikawa and T. Miyake, *Small Sci.*, 2021, **1**, 2100069.

23 S. R. de Groot, P. Mazur and S. Choi, *Phys. Today*, 1963, **16**, 70–71.

24 S. Duhr and D. Braun, *Proc. Natl. Acad. Sci. U. S. A.*, 2006, **103**, 19678–19682.

25 F. Huang, P. Chakraborty, C. C. Lundstrom, C. Holmden, J. J. G. Glessner, S. W. Kieffer and C. E. Lesher, *Nature*, 2010, **464**, 396–400.

26 S. Chapman, T. G. Cowling and D. Park, *Am. J. Phys.*, 1962, **30**, 389.

27 C. Guy and J. Schott, *Appl. Geochem. Supplement.*, 1992, **1**, 33–40.

28 C. C. Tanner, *Nature*, 1952, **170**, 34–35.

29 M. A. Rahman and M. Z. Saghir, *Exp. Therm. Fluid Sci.*, 2013, **49**, 31–39.

30 K. Nishiyama, H. Watanabe and H. Gijutsu, *Hyomen gijutsu*, 1997, **48**, 393–399.

31 H. Watanabe, *Hyōmen gijutsu*, 2007, **58**, 92.

32 F. Muench, *ChemElectroChem*, 2021, **8**, 2993–3012.

33 S. Y. Jun, J. H. Bang, M. S. Kim, D. G. Han, T. Y. Lee and S. Yoo, *Materials*, 2023, **16**, 1739.

34 A. A. Mashentseva, M. A. Ibragimova, S. B. Akhmetova, A. L. Kozlovskiy, M. V. Zdorovets and Z. T. Amirkhanova, *Chem. Pap.*, 2020, **74**, 2189–2199.

35 M. Yasuto and E. Kenkyū, *Earozoru kenkyū*, 2017, **32**, 157–161.

36 N. Kato and R. Kondo, *Jpn. J. Appl. Phys.*, 2018, **57**, 03EK03.

37 W. Lu, M. Winding, M. Lakonishok, J. Wildonger and V. I. Gelfand, *Proc. Natl. Acad. Sci. U. S. A.*, 2016, **113**, E4995.

38 L. Pieuchot, J. Lai, R. A. Loh, F. Y. Leong, K.-H. Chiam, J. Stajich and G. Jedd, *Dev. Cell*, 2015, **34**, 410–420.

39 K. Kikuchi and O. Mochizuki, *PLoS One*, 2015, **10**, e0144938.

40 K. Kono, Y. Saeki, S. Yoshida, K. Tanaka and D. Pellman, *Cell*, 2012, **150**, 151–164.

41 S. Wang, M. V. Shcherbii, S.-P. Hirvonen, G. Silvennoinen, M. Sarparanta and H. A. Santos, *Commun. Chem.*, 2024, **7**, 181.

42 N. Pathak, C. A. Patino, N. Ramani, P. Mukherjee, D. Samanta, S. B. Ebrahimi, C. A. Mirkin and H. D. Espinosa, *Nano Lett.*, 2023, **23**, 3653–3660.

43 A. Prevc, A. Bedina Zavec, M. Cemazar, V. Kloboves-Prevodnik, M. Stimac, V. Todorovic, P. Strojan and G. Sersa, *J. Membr. Biol.*, 2016, **249**, 703–711.

44 B. Zhang, B. Liu, Z. Wu, K. Oyama, M. Ikari and H. Miyake, *Anal. Chem.*, 2024, **96**, 8349–8355.

45 Z. Yu, W. Zhang, J. Zhao, W. Zhong, J. Ren, M. Wu, Z. Zhang, D. Pang, Y. Zhao and G. Chen, *Adv. Funct. Mater.*, 2017, **27**.

46 Z. Zhang, C. Xiao, T. Yong, X. Yang, L. Gan and Z. Li, *Chem. Commun.*, 2020, **56**, 6171–6188.

47 W. Sun, P. Xu, P. Pan, S. Guo, R. Liu, G. Ji, H. Hu, W. Li and L. Dai, *Cancer Nanotechnol.*, 2023, **14**, 82.